RSC Applied Interfaces

ROYAL SOCIETY OF CHEMISTRY

PAPER

View Article Online
View Journal | View Issue

Cite this: *RSC Appl. Interfaces*, 2025, **2**, 1435

Mechanistic insights into the photocatalytic and electrocatalytic activities of $MgNiO_2$: role of reactive oxygen species and oxygen vacancies†

Sandhyawasini Kumari,[ab] Amrita Tripathy,[ab] Vishalakshi Gurumurthy DileepKumar, *[ac] Afaq Ahmad Khan, [ad] Ashoka Siddaramanna,[e] John Kiwi,[f] Mysore Sridhar Santosh,*[ab] Sami Rtimi, *[f] Khushwant Singh[g] and Sai Smaran S. B.[h]

Granular $MgNiO_2$ has emerged as a promising catalyst owing to its remarkable electrocatalytic activity and photodegradation efficiency under visible light. In this work, granular surface-engineered $MgNiO_2$ nanoparticles were synthesized using the precipitation method. The interaction of Mg and Ni, forming Mg–Ni–O structures during high-temperature $MgNiO_2$ synthesis, was investigated through X-ray photoelectron spectroscopy (XPS) analysis. The presence of Ni^{3+} species in the ionic form indicated charge transfer reactions in the catalyst. The band gaps of the as-prepared $MgNiO_2$ and NiO were determined to be 2.2 eV and 3.7 eV, respectively. The first-order transverse optical (TO) phonon modes observed at 536 cm^{-1} indicated the presence of NiO, which was identified as the primary contributor to the Raman peaks. Further, the photocatalytic degradation of caffeine under visible light achieved a removal efficiency of 95.5% within 180 minutes. The intermediate reactive oxidative species (ROS) leading to $MgNiO_2$ degradation were identified, and their lifetime and diffusion length in the solution were reported. Superoxide ($O^{2-\bullet}$) and hydroxyl ($^{\bullet}OH$) radicals were identified as the main ROS contributing to caffeine degradation. The electrocatalytic oxygen evolution reaction (OER) indicated a high density of oxygen vacancies in $MgNiO_2$ compared to NiO, suggesting the promoter role of Mg species in the photocatalyst. These insights provide a holistic understanding of $MgNiO_2$ as a catalyst and its pivotal role in green and efficient caffeine photodegradation and the electrocatalytic OER.

Received 11th April 2025,
Accepted 14th July 2025

DOI: 10.1039/d5lf00102a

rsc.li/RSCApplInter

1. Introduction

Caffeine, a widely used psychoactive substance, can enter natural water sources through wastewater discharge. As a widely consumed psychoactive drug found in coffee, tea and various products, caffeine is frequently detected in surface water and wastewater due to its high water solubility and poor biodegradability. Unlike coloured dyes, caffeine is colourless, avoiding light absorption interference in photocatalytic tests. Its known degradation pathways and easy detection by UV-vis spectroscopy and HPLC further support its use. Despite its benefits at low doses, excessive caffeine can cause health issues such as DNA inhibition, bone loss, cardiovascular risks, and ecological toxicity, making its removal from water essential.

Caffeine has been reported to be only partially degraded in secondary biological wastewater treatment plants (WWTPs) and passes consequently into lakes, rivers and the sub-surface underground streams. The persistence of caffeine in water bodies has been observed to increase steadily in natural ecosystems over the past few decades. Some articles have recently addressed the methods used to degrade caffeine.[1–3] Furthermore, caffeine in relatively high concentrations is difficult to degrade through secondary biological wastewater treatment in municipal treatment

[a] *Coal to Hydrogen Energy for Sustainable Solutions (CHESS) Division, CSIR–Central Institute of Mining and Fuel Research (CIMFR), Digwadih Campus, PO: FRI, Dhanbad-828108, Jharkhand, India. E-mail: santoshms@cimfr.res.in, deepuvg29@gmail.com*
[b] *Academy of Scientific and Innovative Research (AcSIR), Ghaziabad-201002, India*
[c] *Department of Chemistry, HKBK College of Engineering, Bangalore-560045, Karnataka, India*
[d] *GreenCat Lab, Department of Chemical Engineering, Indian Institute of Technology (ISM), Dhanbad-826004, Jharkhand, India*
[e] *Department of Chemistry, School of Applied Sciences, REVA University, Bangalore-500064, Karnataka, India*
[f] *Global Institute for Water Environment and Health, 1201 Geneva, Switzerland. E-mail: rtimi.sami@gmail.com*
[g] *Department of Chemistry, Pradhanmantri College of Excellence, SLP Govt PG College, Morar, Gwalior-474006, Madhya Pradesh, India*
[h] *Sai Smaran S.B., Duke University, Box 90300, Hudson Hall, Durham, NC 27708-0287, USA*

† Electronic supplementary information (ESI) available. See DOI: https://doi.org/10.1039/d5lf00102a

plants. Therefore, the need to explore new technical approaches to degrade caffeine is highly imperative. Recently, electro-Fenton, anodic oxidation, and light-activated processes have been reported to lead to caffeine degradation.[4–6] Photocatalysis is a highly promising water treatment technology[7,8] and appears to suit this objective. In this process, illumination prompts the excitation of photocatalysts, generating electron–hole pairs directly. The efficiency hinges on the recombination rate or lifetime of these pairs; faster recombination translates to a shorter reaction time. Photoluminescence (PL) spectra are vital for probing this recombination rate.

In the past decade, heterogeneous photocatalysis significantly advanced solar energy conversion and improved environmental remediation, garnering widespread attention. Future mass production necessitates the meticulous selection of environmentally friendly, cost-effective, and potent photocatalysts for practical applications, which plays a pivotal role in the development of advanced oxidation processes. Moreover, several countries have reduced the permissible levels of caffeine in drinking water.[9] Thus, innovative photocatalytic materials should be explored to increase the degree of water quality.[6]

In the photodegradation of organic compounds by a photocatalyst, three primary reaction pathways are envisaged: photocatalysis, photolysis, and dye photosensitization. During photolysis, a photoinduced electron directly interacts with O_2, generating singlet oxygen ($^1O_2$) as an oxidant for the subsequent photolysis of the organic compound, outlining key mechanisms in the process.[10,11] Nanomaterials, with their dual functionality as photocatalysts and electrocatalysts, have been recently explored for energy conversion and storage.[12,13] One such material, $MgNiO_2$, has found applications in processes related to methane reforming, sensors, supercapacitors, H_2 storage, and environmental cleaning. Recent work has also explored $MgNiO_2$ for sensing applications due to its flower-structured flakes with high porosity.[14]

Another application of $MgNiO_2$ is in gas separation membranes, where its incorporation into mixed matrix membranes (MMMs) has revolutionized gas permeation performance. When embedded in a polysulfone (PSf) matrix,[15] $MgNiO_2$ nanoparticles introduced nanoscale voids, facilitating faster gas transport and selective gas permeation while improving the membrane stability and efficiency. Beyond its role in catalysis, $MgNiO_2$ has shown remarkable potential in lithium-metal batteries.[16,17] Its incorporation as a ceramic additive improves the protective film quality on lithium anodes, significantly reducing interfacial resistance and enhancing cycling stability. Additionally, $MgNiO_2$-based composites have been explored in zinc-ion hybrid supercapacitor batteries (ZHSBs), where its hollow microsphere morphology facilitates fast ion insertion and extraction, contributing to a high energy density of 157–89 Wh kg^{-1} and a long-term cycling stability of 10 000 cycles with 97% retention. Further, a critical application of $MgNiO_2$ is in hydrogen storage. Incorporating $MgNiO_2$ into MgH_2 significantly lowers the hydrogen desorption temperature,[18] improves absorption kinetics, and enhances storage capacity by facilitating synergetic catalytic effects. Additionally, its high electrochemical stability and superior capacitance retention make it an ideal supercapacitor electrode material.

Hydrothermal preparation to synthesize $MgNiO_2$ in the form of chrysanthemum flowers (CFs) has been reported to show effective sensing characteristics. The Ni-ions in the flower-like $MgNiO_2$ presented multiple Ni^{3+}/Ni^{2+} oxidation states inducing the electronic behavior.[19] Chrysanthemum flower-like nanostructured $MgNiO_2$ electrodes have also been recently reported for the removal of Hg^{2+} ions in an aquatic medium.[14] $MgNiO_2$ has been synthesized using different methods, and different morphologies have been identified. Many factors such as pH, surfactant, and calcination temperature affect the morphology during the precipitation process. A pH of 7 to 9 would be more favourable for obtaining granular morphology.

This work focuses mainly on the preparation of granular $MgNiO_2$ to degrade caffeine under visible light irradiation. This material also shows an electrocatalytic oxygen evolution reaction (OER). Linear sweep voltammetry (LSV) and Tafel slopes have been employed to determine the kinetics, rate of the OER and the reaction mechanism. The $MgNiO_2$ synthesis was designed in such a way that a large surface area is avoided similar to flakes. This prevents significant adsorption of pollutants in the aqueous phase while enabling catalytic and photocatalytic surface processes to proceed. This work presents a detailed study of the $MgNiO_2$ surface and the photoinduced degradation kinetics for caffeine. The mode of intervention of the reactive oxygen species (ROS) in solutions during caffeine degradation is addressed herein. Considering the above-mentioned aspects, this work provides better insights and an understanding of the photocatalytic degradation process and the oxygen evolution reaction mediated by $MgNiO_2$.

2. Experimental section

2.1. Synthesis of $MgNiO_2$

The synthesis of $MgNiO_2$ nanoparticles was carried out following a procedure reported in a previous article.[15] In brief, granular surface-engineered $MgNiO_2$ nanoparticles were prepared by mixing 0.1 moles of magnesium nitrate hexahydrate ($Mg(NO_3)_2{\cdot}6H_2O$, 98%) and nickel nitrate hexahydrate ($Ni(NO_3)_2{\cdot}6H_2O$, 99%) in 50 mL of deionized water at room temperature. To this mixture, a sodium hydroxide (NaOH, 98%) solution was added in a ratio of 1/1/2. The addition of the sodium hydroxide solution resulted in a precipitate, which was then left undisturbed for 6 h for complete precipitation. The solution was thoroughly washed with deionized water to remove impurities and dried in air. The solid precipitate was then calcined at 650 °C for 3 h.

2.2. Material characterization

The crystalline composition of the catalyst was analyzed *via* powder X-ray diffraction (PXRD) using a Bruker D8 Advance

Eco X-ray diffractometer equipped with a Cu-Kα radiation source (λ = 1.54 Å) at a scan rate of 2° min^{-1}. X-ray diffraction was performed using an automated multipurpose XRD system equipped with a high-accuracy theta–theta goniometer featuring a horizontal sample mount and an expert system guidance software (Model: SmartLab X-ray diffractometer; Make: Rigaku, Japan) with Cu $K\alpha_1$ radiation (λ: 1.5406 Å). An X-ray tube generator was operated at 40 kV and 45 mA. The measurements were performed in a theta/2-theta (Bragg–Brentano focusing, D/teX) geometry for absolute 2θ scan range between 10° and 80° with a scan step of 0.01° and a scan speed of 10.40182° min^{-1} in the continuous mode. The sample was rotated in a beta-stage to obtain accurate intensities. To identify the chemical bonds present in $MgNiO_2$, Fourier transform infrared (FTIR) spectroscopy measurements were performed using a Shimadzu IRAffinity-1S spectrophotometer. Field-emission scanning electron microscopy (FESEM; Carl Zeiss Model Supra 55) was employed to study the morphology of the as-synthetized $MgNiO_2$ nanoparticle. The surface composition and oxidation states of $MgNiO_2$ components were analyzed by X-ray photoelectron spectroscopy (PHI III Scanning XPS Microprobe). The surface area was determined by the Brunauer–Emmett–Teller (BET) method (Quantachrome Autosorb iQ2). Total organic carbon (TOC) was measured using Aurora 1030 (O.I. Analytica). A confocal micro-Raman spectrometer (Seki Technotron Corporation, Japan) was adopted in a backscattering geometry to record the Raman spectra with a He–Ne laser (wavelength 633 nm) and used as an excitation source. Transmission electron microscopy (TEM; JEOL/JEM 2100 200 kV) analysis was performed to understand the structure and elemental distribution of $MgNiO_2$. A Shimadzu UV-visible spectrophotometer (equipped with an ISR-3100 integration sphere) was used to study the absorption of the prepared $MgNiO_2$ nanoparticle.

2.3. Photodegradation experiments

Samples were irradiated with a 50 W LED visible light (OPPLE LED B22 Base, 50 W, 5000 Lumen, 6500 K). In each experiment, a volume of 100 mL of the solution was used. The pH of the reaction was adjusted by adding NaOH and HNO_3. During the systematic investigation of the parameters controlling the photodegradation kinetics of caffeine, the concentration of the caffeine was varied between 10 and 40 mg L^{-1}. The quenching experiments

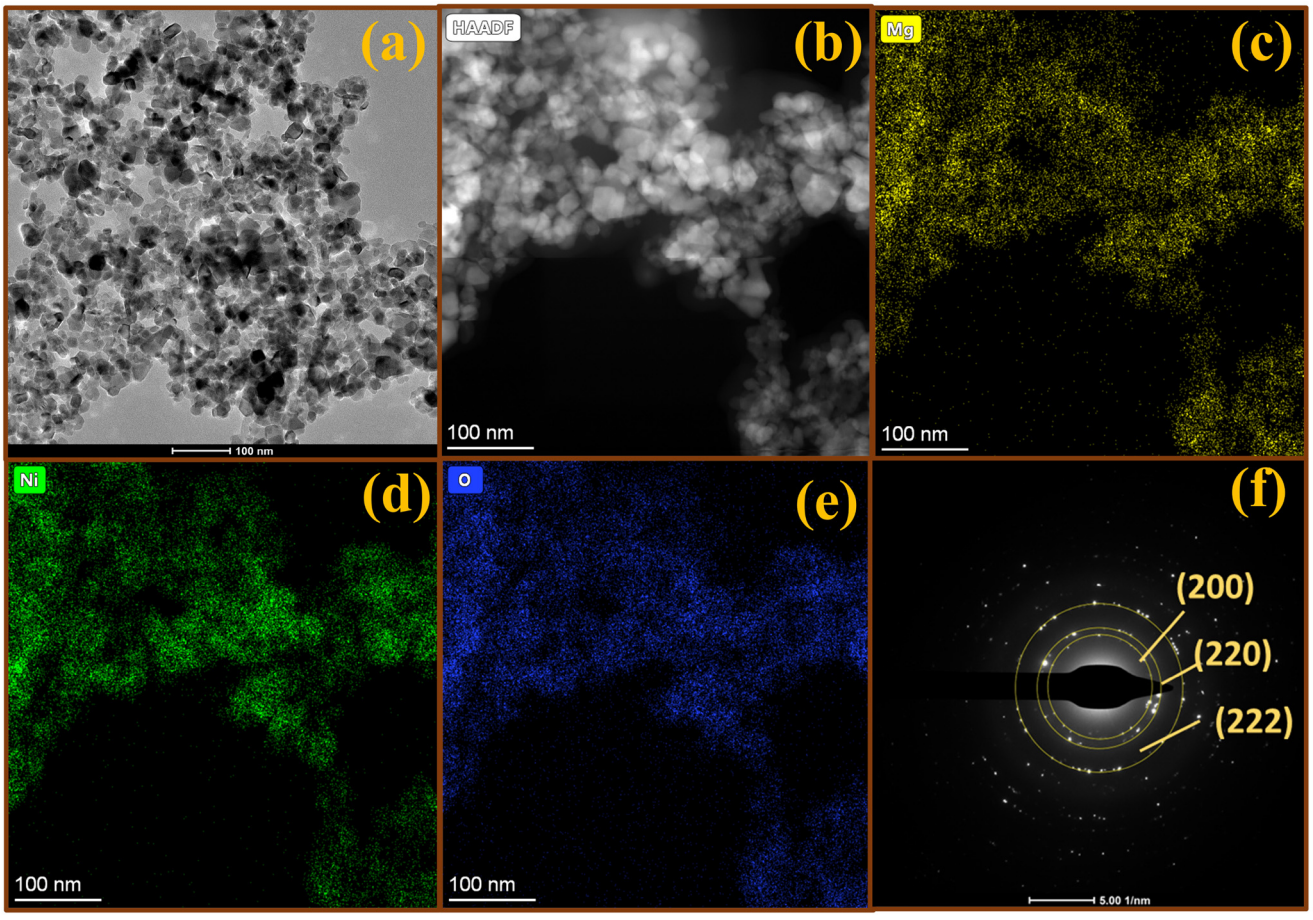

Fig. 1 (a) TEM micrographs of the $MgNiO_2$ particles representing the well-ordered crystalline structure. (b) HAADF image of the $MgNiO_2$. (c–e) Atomic mapping of Mg, Ni and O. (f) SAED patterns of the $MgNiO_2$ nanoparticles.

were carried out at the initial pH of the caffeine solution. At pre-set time intervals, 2 mL of the irradiated solution was collected, filtered using 0.22 mM filter paper to ensure no solid particles remained in the solution and then analyzed. The caffeine concentration during the photodegradation reaction was determined using a UV-vis spectrometer.

2.4. Preparation of nickel foam electrode for the OER

To assess the electrocatalytic activity of the synthesized $MgNiO_2$ for the OER, a three-electrode system was employed. The working electrode was prepared by a drop-casting method on a nickel foam (NF) substrate. Initially, NF was cleaned with HCl and distilled water to remove impurities. Subsequently, 2 mg of the catalyst material was mixed with an ethanol–water solution and sonicated for 20 min to ensure uniform distribution. This mixture was then drop-cast onto the NF. An Ag/AgCl electrode was used as the reference electrode, while platinum was employed as the counter electrode.

3. Result and discussion

3.1. Microstructure of $MgNiO_2$ using electron microscopy

To observe the morphology of $MgNiO_2$, field-emission scanning electron microscopy (FE-SEM) was used. The observations are shown in Fig. S1.† It confirms the presence of spherically aggregated particles with diameters ranging from 0.5 to 1 μm. Significant agglomeration occurs due to the high-temperature calcination performed at 650 °C, employed during the catalyst synthesis. The energy-dispersive X-ray (EDX) spectra of $MgNiO_2$ shown in Fig. S1† indicate the surface percentage atomic composition of O = 51.9%, Mg = 28.6% and Ni = 19.5%. The analysis reveals the presence of Mg, Ni, and O elements in an atomic percentage ratio of approximately 1/1/2 consistent with the expected elemental distribution of $MgNiO_2$. In the EDS spectrum, no other elemental peaks are observed, suggesting the purity of the synthesized $MgNiO_2$.

To further analyze the morphology of the synthesized nanoparticles, the TEM micrographs of $MgNiO_2$ were taken by dispersing the catalyst in EtOH and drop-cast onto a copper grid. The TEM micrographs shown in Fig. 1 display the well-distributed granular-shaped nanoparticles with irregular edges of the catalyst. These edges of particles indicate a well-ordered crystalline structure obtained in a controlled growth environment during the synthesis. For the sake of comparison, the TEM micrographs of NiO from the literature were used as a reference, which reveal the formation of agglomerates, resembling the $MgNiO_2$ clusters, indicating similar structural characteristics.[20] The STEM-EDS (Fig. 1b–e) mapping was performed to investigate the sample's composition, providing evidence for the presence of Mg, Ni and O in the as-prepared material. The micrographs display the uniform distribution of Mg, Ni and O, whereas

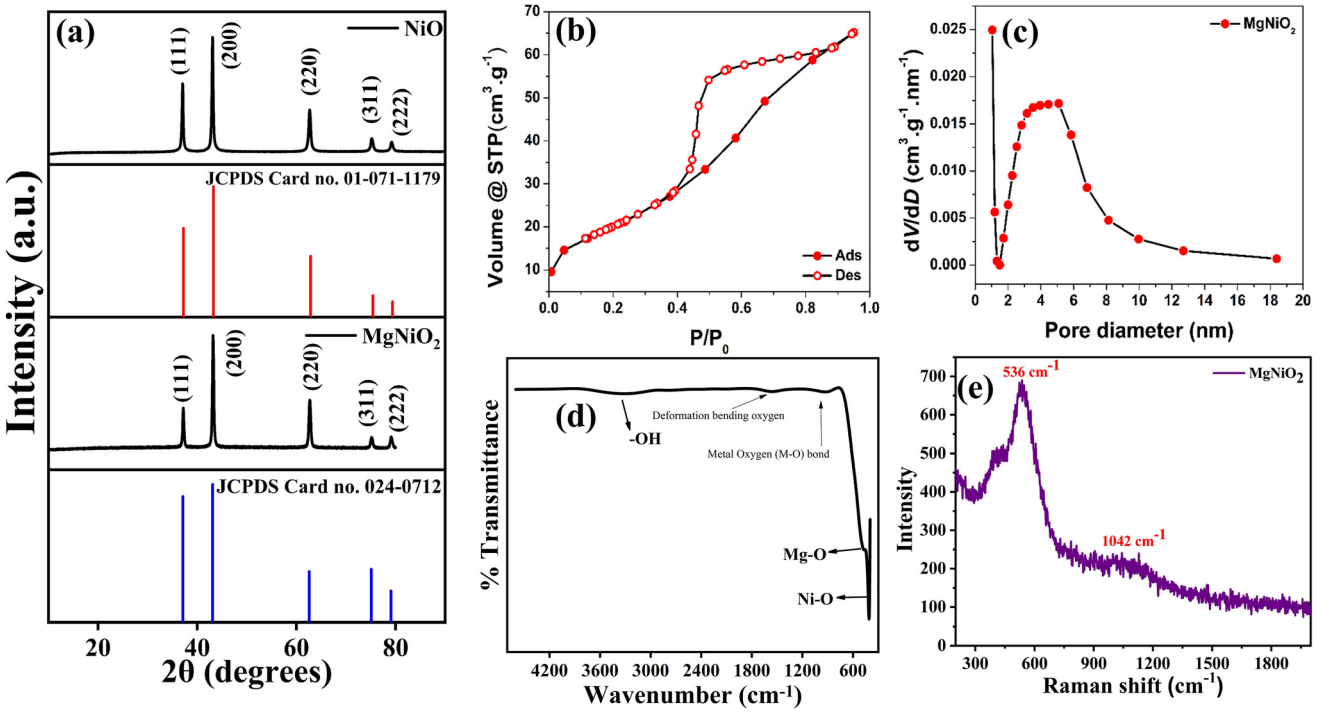

Fig. 2 (a) Powder XRD patterns of the $MgNiO_2$ and NiO crystals indicating the crystalline nature of the synthesized materials. Crystal planes have been referenced using the JCPDS database and match well with the synthesized materials. (b) N_2 adsorption–desorption isotherm. (c) Pore size distribution plots. (d) FTIR spectrum indicating the oxide bonding wavelength position of the material components. (e) Raman spectra of the as-prepared $MgNiO_2$ particles.

the SAED pattern shows the polycrystalline nature of the prepared $MgNiO_2$ nanoparticles (Fig. 1f).

3.2. Powder X-ray diffraction of $MgNiO_2$ crystals

The powder XRD patterns of $MgNiO_2$ and NiO crystals are depicted in Fig. 2a. The peaks shown in Fig. 2a were referenced to the cubic phase and spinel structure of the corresponding peaks of $MgNiO_2$ and NiO, and they align well with the JCPDS File No. 024-0712 and 071-1179, respectively. The polycrystalline structures observed in the HRTEM images align well with the PXRD data of the catalyst, which display sharp peaks indicating its polycrystalline nature.

The average crystallite size was estimated from the broadening of the diffraction peaks by the Scherrer method.[21] The Scherrer equation in eqn (1) relates the size of sub-micrometre crystallites with the observed peak broadening obtained during the XRD diffraction runs.

$$D = k\lambda/\beta\cos(\theta) \quad (1)$$

where 'β' is the complete broadening of half maxima of the diffraction peaks and 'θ' is the diffraction angle. The average crystallite size was determined by analyzing the broadening of the diffraction peaks. The atomic radius of the hexagonal Ni of 0.124 nm and that of the hexagonal Mg of 0.160 nm are close[7] to each other, allowing the diffusion of both elements at the high temperature employed during the $MgNiO_2$ preparation. Some preparative methods have been reported recently for $MgNiO_2$, reflecting the interest in this material for diverse applications.[22]

3.3. Surface area, Fourier transform infrared (FTIR) and Raman spectra of the as-prepared $MgNiO_2$ nanoparticles

The specific surface area and pore size distribution of $MgNiO_2$ were systematically investigated by N_2 adsorption–desorption isotherm analysis. Before the analysis, the sample was degassed at 130 °C for 6 h to ensure optimal conditions. The BET-specific surface area (S_{BET}) of $MgNiO_2$ derived from the isotherm data was determined to be 72.5 $m^2\ g^{-1}$ (Fig. 2b). By employing the Barrett–Joyner–Halenda (BJH) method, the average pore width was calculated as 3.96 nm, with a corresponding pore volume of 0.104 $cm^3\ g^{-1}$, as shown in Fig. 2c. These findings suggest that $MgNiO_2$ possesses ample active sites, making it an efficient catalyst for pollutant degradation and oxygen evolution. The surface area is desirable for catalytic materials intervening in photocatalysis/electrocatalysis since they would provide an adequate number of surface catalytic sites but concomitantly present reduced surface area/porosity.[23] The pore width falls within the mesoporous range of 2–50 nm. This structural feature enhances the availability of active sites and promotes efficient mass transport, making $MgNiO_2$ an effective catalyst for pollutant degradation and the oxygen evolution reaction. A reasonable pore volume provides sufficient space for reactant accommodation and rapid diffusion. It contributes to maintaining an accessible porous network, promoting continuous reaction cycles without pore blockage. This is the required characteristic for a photocatalyst, providing effective reactive sites to carry out the photocatalysis, but does not allow excessive absorption of the pollutant to be degraded, blocking the catalytic sites. These sites involve unpaired electrons, defects or specific chemical groups that can interact with the molecules to be degraded. The accumulation of caffeine on the surface-active photocatalytic sites would preclude caffeine degradation.

The FTIR spectrum of the $MgNiO_2$ sample displayed in Fig. 2d shows a vibrational frequency at 3433 cm^{-1} corresponding to the vibrational frequency of –OH bonds. The moisture on the sample's surface leads to the absorption of surface water molecules on $MgNiO_2$, giving rise to the observed –OH bond peak. The –OH bond peak is derived from surface water rather than structural chemical bonds within $MgNiO_2$. The peak at 519 cm^{-1} arises from the vibrational bond frequency of Mg–O,[24] while the peak at 443 cm^{-1} is associated with the vibrational bond frequency of Ni–O.[25] The peaks shown in Fig. 2d observed for the $MgNiO_2$ sample agree well with that of the literature ref. 26. The peak at 939 cm^{-1} likely corresponds to the metal–oxygen (M–O) stretching vibration bonds of Mg and Ni, since both are bonded to oxygen and involve stretching of the bonds between the metal ions and oxygen. The peak at 1563 cm^{-1} is associated with the bending vibrations of oxygen atoms. This is linked to the oxide-structure deformation or the bending of oxygen atoms in $MgNiO_2$.

The Raman spectroscopy findings of $MgNiO_2$ are given in Fig. 2e. A peak observed at 536 cm^{-1} can be attributed to first-order transverse optical (TO) phonon modes, while the peak at 1042 cm^{-1} could have originated from longitudinal optical (LO) phonon modes. The significant presence of NiO in the sample probably plays a crucial role in the emergence of these distinct Raman peaks, highlighting its influence on the vibrational dynamics of $MgNiO_2$. Moreover, the results from the Raman spectra suggest that the catalyst $MgNiO_2$ not only exhibits a substantial degree of phase purity but also reflects well-defined phonon behaviour, which is essential for its potential applications in catalytic processes.[27] The 536 cm^{-1} Raman peaks in $MgNiO_2$ appears higher than the typical TO phonon modes of pure NiO and MgO (446 cm^{-1}). The shift in the Raman peak to 536 cm^{-1} can be explained by modifications in the lattice dynamics caused by the coexistence of Mg^{2+} and Ni^{2+} cations. This mixed-cation environment alters the bond strengths within the crystal, increasing the force constants and consequently increasing the phonon frequencies.[28] The 1042 cm^{-1} peak lies close to the 2LO mode of NiO (1009 cm^{-1}) and the surface mode of MgO (1080 cm^{-1}), suggesting that it probably originates from a second-order phonon process or a surface-related

vibrational mode influenced by Mg–Ni interactions in the mixed oxide lattice.[14,29]

3.4. X-ray photoelectron spectroscopy (XPS) and spectral absorption of the as-prepared $MgNiO_2$ nanoparticles

Fig. 3 shows the XPS deconvolution of the major peaks of $MgNiO_2$. The presence of $Mg(OH)_2$, as shown in Fig. 3a, indicates the existence of hydroxide groups on the surface of the photocatalyst, in some sub-oxide forms of MgO. In agreement with these data, Mg^{2+} seems to be the main component in MgO.

The Ni 2p peaks in Fig. 3b indicate the presence of Ni^{2+} in $MgNiO_2$. The binding energy of Ni $2p_{3/2}$ in the peak at 861.7 eV (satellite peak) was found to be Ni(III) oxyhydroxide (NiOOH), an oxidation state corresponding to Ni^{+3}. This provides evidence for higher Ni^{3+} states in the $MgNiO_2$ structure that can only proceed through Mg–O–Ni formation during the catalyst synthesis.

The spin–orbit splitting values (Δ) for Ni^{2+}/Ni^{3+} are:

$$\Delta = 872.74 - 855.13 = 17.61 \text{ eV for } Ni^{2+} \text{ and } \Delta = (874.21 - 856.60) = 17.61 \text{ eV for } Ni^{3+}$$

Oxygen vacancies play an important role in promoting Ni and Mg ionic species in the crystal structure of $MgNiO_2$. A high density of oxygen vacancies was found in $MgNiO_2$ by electrocatalytic OER studies and is presented in the last section of this study. Mg has recently been reported as a promoter in reactions catalyzed by natural clay-based Ni-catalysts by boosting the dry reforming of methane (DRM).[30]

Different forms of oxygen-containing species were observed in $MgNiO_2$ like (–OH), surface absorbed oxygen (O_2^-) and surface lattice oxygen, as shown in Fig. 3c. The 1s deconvolution confirms the presence of oxygen vacancies[31] in $MgNiO_2$, modifying the electronic properties and reactivity of the material. According to the reported literature data, the binding energy range for oxygen vacancies in $MgNiO_2$ lies between 530 and 537 eV. Peaks above 530 eV are characteristic of O^{2-} anions in $MgNiO_2$, whereas peaks above this range correspond to oxygen vacancies. The percentage of oxygen vacancies in $MgNiO_2$ particles was estimated to be 22% by integrating the areas of peaks. Correlating the 22% oxygen vacancies identified in $MgNiO_2$ through XPS with the EDS results showing 54.2 atm% of oxygen, the oxygen vacancies represent 11.9% of the total oxygen content of the $MgNiO_2$ material. This is huge and can explain the photocatalytic activity of the material.

3.5. Diffuse reflectance spectroscopy of NiO and $MgNiO_2$ and photoluminescence spectrum of $MgNiO_2$

Diffuse reflectance spectra (DRS) of NiO and $MgNiO_2$ were obtained to determine the light absorption and band gap values. It is readily seen that $MgNiO_2$ and NiO absorb light in the UV-near visible range, as shown in Fig. 4a. The Kubelka-Munk plots allowed us to estimate the bandgaps of NiO (4.12 eV) and $MgNiO_2$ (2.39 eV) and the results obtained by the interpolation are shown in Fig. 4b and c. A weak peak at 3.42 eV appeared for NiO, justifying a light absorption edge of 362 nm. For $MgNiO_2$, the peak at 1.5 eV indicates the possibility of light absorption of this material up to 826 nm. These observed variable bandgaps could be due to the transfer of electrons from the O 2p valence band to the Ni 3d conduction band and the other bandgap observed can be attributed to the presence of oxygen vacancies and/or the intermediate energy levels within the bandgap. These bandgaps justify the semiconductor behavior of both metal oxides.

Fig. S2† shows the photoluminescence (PL) studies of an aqueous suspension of $MgNiO_2$, performed at different excitation wavelengths (λ_{ex}) ranging from 280 to 600 nm at room temperature. It is observed from the PL spectra at λ_{ex} of 330 nm that the maximum emission wavelength (λ_{em}) is 389 nm. When the λ_{ex} value increases, the λ_{em} values are red-shifted, and at λ_{ex} of 400 nm, a λ_{em} value of 460 nm is observed. The presence of a single, well-defined peak in the emission spectra indicates a uniform distribution of particles within the aqueous suspension, suggesting homogeneity in their size and optical properties. Further, the pronounced and broad peaks observed in the PL spectra result from the direct recombination of electrons from the conduction band

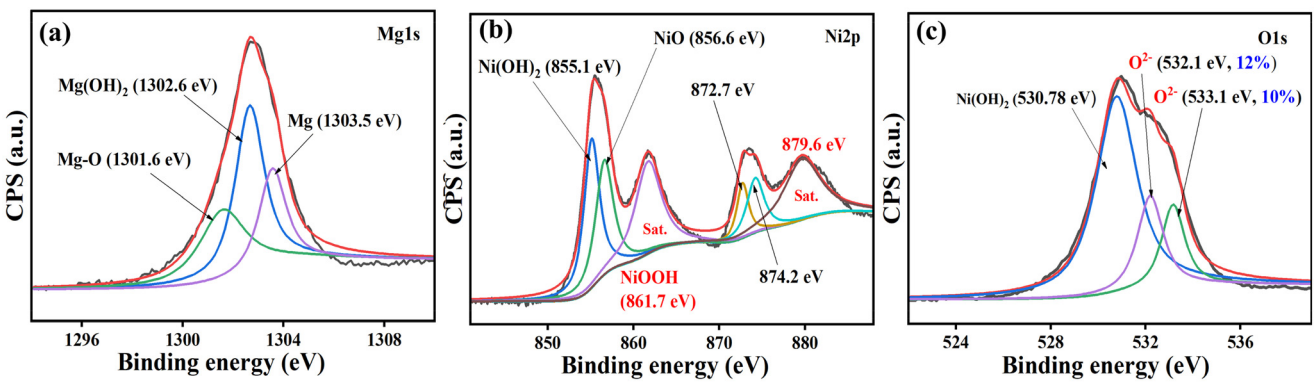

Fig. 3 Oxidation states of the synthesized catalyst by XPS deconvolution of (a) Mg 1s, (b) Ni 2p, and (c) O 1s in the prepared $MgNiO_2$.

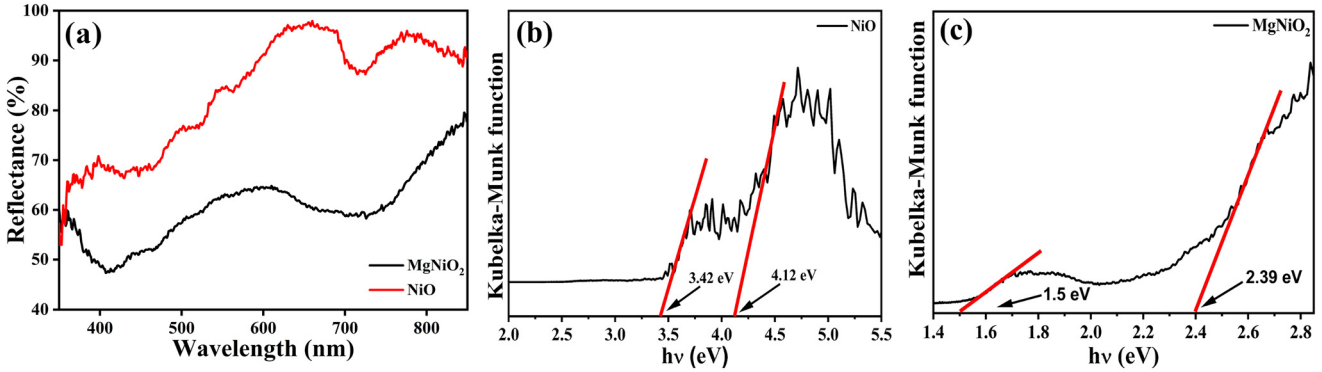

Fig. 4 (a) Diffuse reflectance spectroscopy (DRS) spectra of NiO and $MgNiO_2$. (b) Photoluminescence spectra of an aqueous suspension of $MgNiO_2$ at different excitation wavelengths. (c) Tauc plots of NiO and $MgNiO_2$ noting the respective bandgaps of these materials.

with holes in the valence band. This direct recombination process is crucial for understanding the material's photophysical behaviour and suggests efficient energy transfer mechanisms at play within the $MgNiO_2$ system.

3.6. Photocatalytic degradation of caffeine, reaction mechanisms, kinetics and identification of the ROS-radicals intervening in the photodegradation process

Fig. 5a–d show the photodegradation of caffeine in an aqueous solution determined by UV-vis spectroscopy. Fig. 5a shows the photodegradation of caffeine under light (photolysis) followed by the introduction of NiO and $MgNiO_2$ under visible light irradiation (LED lamp source: 50 W). Fig. 5b shows the results as a function of the amount of caffeine concentration by the $MgNiO_2$ catalyst. Fig. 5a clearly illustrates the significant role played by the catalyst and light in the degradation process of caffeine. In the absence of the catalyst, the degradation of caffeine was observed to be 7.85% under light irradiation. In comparison, when employing the NiO catalyst, the degradation increased notably to approximately 60.45%, indicating a substantial impact of the catalyst. However, upon introducing the primary catalyst $MgNiO_2$, the degradation enhanced significantly to 95.4%, highlighting the effectiveness of the catalyst in the degradation process of caffeine.

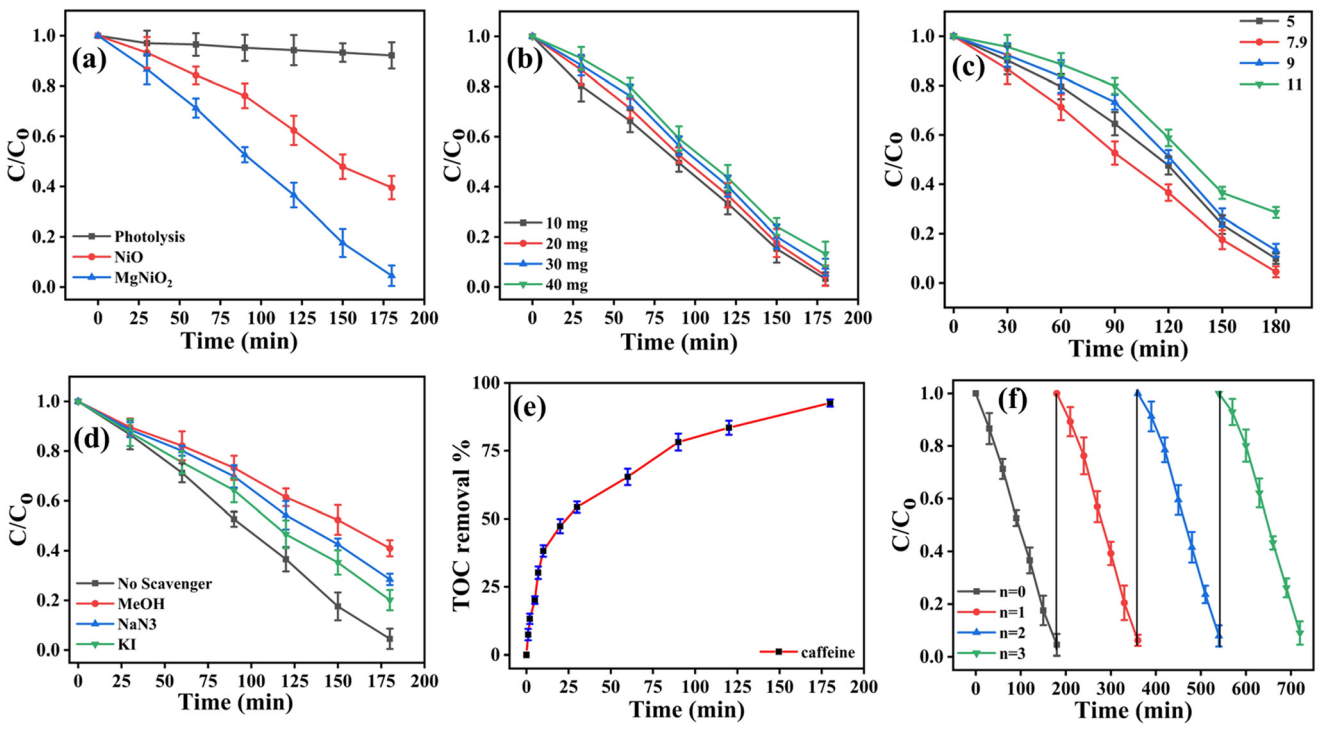

Fig. 5 Photocatalytic degradation of caffeine under visible light irradiation: (a) under light, NiO, and $MgNiO_2$; (b) as a function of the amount of pollutant used; (c) effect of pH on caffeine degradation; (d) in the presence of specific ROS scavengers; (e) TOC removal over a period of time and (f) repetitive cycling of caffeine photodegradation up to the fourth cycle for all studies (all experiments were performed in triplicate).

To further comprehend the influence of pollutant concentration on caffeine degradation, concentrations ranging from 10 to 40 ppm were investigated. Notable differences were not observed between the 10 and 20 ppm concentrations of the pollutant. However, a decrease in degradation was noted when the concentration was increased to 30 ppm and 40 ppm (Fig. 5b). This phenomenon may be attributed to the likelihood of increased pollutant concentration obstructing light penetration, thereby affecting the overall degradation process.

Fig. 5c shows the photocatalytic degradation of caffeine under different pH conditions ranging from 5 to 11. The aqueous pH (7.9) was found to be most effective for the degradation of caffeine under visible light using the synthesized catalyst $MgNiO_2$. At this initial pH, the degradation reached 95.47%, showcasing optimal conditions for the process. As the reaction conditions varied from the initial pH, a decrease in the degradation was observed. The efficiency of caffeine degradation is primarily influenced by the degree of ionization of caffeine and the characteristics of the catalyst. Considering the weakly acidic nature of caffeine with a dissociation constant of 8.3, the initial pH proves to be more favourable compared to acidic or alkaline pH levels for effective degradation under visible light conditions.

The total organic carbon (TOC) provides an insight into the overall degradation or mineralization of organic components, including caffeine, and offers a broader perspective on the degradation process by considering changes in the overall organic content. Hence, using a UV-visible spectrophotometer, real-time monitoring of concentration variations throughout the reaction process was performed, and subsequently, the ultimate concentration of the caffeine solution post-mineralization was determined. An analysis of total organic carbon (TOC) was carried out to validate the efficacy of the mineralization process (Fig. 5d). The calculated TOC removal percentage revealed a substantial efficacy of 92.6%. The high TOC removal percentage supports the conclusion that a significant portion of the organic carbon in caffeine molecules has undergone mineralization, resulting in a cleaner and less carbon-intensive solution.

Fig. 5e illustrates the ROS-mediated photodegradation mechanism, as outlined in reactions (1)–(6). This mechanism highlights the reactive oxygen species (ROS) generated in the solution along with their associated potentials:

The ROS-mediated photodegradation mechanism is suggested next by reactions (1)–(6) noting the ROS generated in solution with their respective potentials:

$$[MgNiO_2] + \text{light} \rightarrow [MgNiO_2]^* \rightarrow \text{caffeine}^+ + (MgNiO_2 cb_e^-) \quad (1)$$

$$(MgNiO_2 cb_e^-) + O_2 + H^+ \rightarrow HO_2^{\bullet} \quad E^0 - 0.05 \text{ NHE} \quad (2)$$

$$MgNiO_2 cb_e^- + O_2\text{ads}^+ \rightarrow O_2\text{ads} \quad E^0\ 0.16 \text{ NHE} \quad (3)$$

$$MgNiO_2^+ + OH^-\text{ads}^+ \rightarrow {}^{\bullet}OH^- \quad E^0\ 1.90 \text{ NHE} \quad (4)$$

$$MgNiO_2^+ + H_2O\text{ads}^+ \rightarrow \cdot OH\text{ads} + H^+ \quad (5)$$

$$O_2^{\bullet -} + H^+ \rightarrow HO_2^{\bullet} \quad (6)$$

In Fig. 5d, methanol is used as a quencher of $^{\bullet}OH$-radicals. KI was used to scavenge the positive vb-holes (vb_{h^+})[32] and NaN_3 was added as the oxygen singlet $^1O_2$ scavenger. Fig. 5d shows that $^{\bullet}OH$-radicals seem to be the most important radical species, leading to caffeine degradation. One should consider that NaN_3 used as an oxygen singlet ($^1O_2$) scavenger also reacts with the $^{\bullet}OH$-radical at a rate close to the rate of the reaction of this scavenger with singlet oxygen.[33] The data reported for $^1O_2$ in Fig. 5d considers the undifferentiated quenching of $^1O_2$ and the $^{\bullet}OH$-radical[34] by NaN_3.

The following section addresses the diffusion length in the solution of the most important radicals since it is a controlling feature of the performance of these radicals during caffeine photodegradation. Taking the reaction rate of the $^{\bullet}OH$-radical with caffeine ($\sim 10^9$ M^{-1} s^{-1}) and the caffeine concentration of $\sim 10^{-4}$ M (caffeine MW 194), the $^{\bullet}OH$ radical diffusion distance (x) away from the $MgNiO_2$ photocatalyst surface can be estimated by taking the reaction rate between $^{\bullet}OH$ and caffeine in aqueous solutions following the simplified Smoluchowski equation.[35,36] The lifetime of the reaction pair made up of $^{\bullet}OH$ radicals and caffeine was estimated using eqn (7):

$$\frac{1}{\tau} = k^{\bullet}\text{OH}[\text{RH}] = 10^5 \text{ s}^{-1} \text{ and } \tau = 10^{-5} \text{ s} \quad (7)$$

The $^{\bullet}OH$-radical mobility/diffusion "x" would be given through the approximation in eqn (8):

$$x^2 = D\tau \quad (8)$$

where D is the average diffusion coefficient value of small radicals/molecules in aqueous solutions ($D \sim 5 \times 10^{-6}$ cm^2 s^{-1}). From these considerations $x = 7 \times 10^{-6}$ cm or 700 Å for the $^{\bullet}OH$ radical. The $HO_2^{\bullet}$ radical diffusion length (x) can also be projected by the Smoluchowski diffusion equation. The $HO_2^{\bullet}$ radical reaction rate has been reported in the range $k = 10^5$–10^7 M^{-1} s^{-1}. In this case, the reaction lifetime of the reaction pair is 10^{-2} s and the diffusion length of the $HO_2^{\bullet -}$ radical is 2.4×10^4 Angstrom.[37,38] Singlet oxygen $^1O_2$ has been reported with a lifetime of 3.6 ms and a diffusion mobility estimated around ~75 nm in the solution, and from the preceding paragraph, the lifetime would be 0.1 ms (see eqn (7)). The difference observed for the lifetimes of these intermediates is because the singlet oxygen is in the gas phase and the $^{\bullet}OH$ radical is a species in solution.[38]

Reactions (2)–(6) allow for two comments pertaining to caffeine photodegradation: (a) that mass transfer does not play a role in the photocatalytic process as known for radical or ion-molecule reactions, and (b) no activation energy is required for ROS radical reactions.

Basically, the reduction in caffeine concentration shown in Fig. 5 consists of the degradation and discolouration of

caffeine. The phenolic caffeine molecule nicotine and aliphatic acids during the caffeine photodegradation are colourless. The coffee stain contains colloidal coloured components. They consist of quaternary amines and cationic surfactants. When roasting coffee beans, functionalities are produced from the transformation of saccharides into caramel. These functionalities can also be generated from the transformation of amino acids into melanoidins and chlorogenic acids (CGA) transforming into quinolactones, melanoidins and humic acids. The phenolic acids present in green coffee beans are mostly chlorogenic acid, a pseudo-tannin, made up of low-molecular-weight hydroxycinnamic and quinic acids (implicated in the perceived acidity of coffee).[39] The results reported in Fig. 5 for the photodegradation/mineralization of caffeine imply the dissociation of allylic and benzylic bonds. Single CH-bonds dissociate at 85–100 kcal mol^{-1}. Caffeine components containing double C–H bonds need up to 174 kcal mol^{-1} bond dissociation energy and triple C–H bonds need a bond dissociation energy >200 kcal mol^{-1}. The high-energy requirements needed to dissociate the multicomponent caffeine is the rationale for the slow photodegradation kinetics presented in Fig. 5d.

Scavenger effects were performed using various other scavengers (Fig. S3†), which provides equally substantial evidence to corroborate the emergence of radicals specifically ROS.[40] Accordingly, diverse scavengers were employed to capture these entities. Sodium oxalate (4 mM) and sodium bicarbonate (4 mM) were introduced into the solution before the photodegradation of caffeine, serving to quench hole (h^+) and hydroxyl radical ($^{\bullet}OH$), respectively. Further, the photodegradation of caffeine was conducted under a nitrogen (N_2) atmosphere to substantiate the production of oxygen free radicals ($O^{2-\bullet}$). The outcomes revealed a significant impact on the photocatalytic efficacy of $MgNiO_2$, which diminished from 95.4% to 86.5% with sodium oxalate, 75.4% with sodium bicarbonate, and 56.4% under N_2. This attenuation in activity provides compelling evidence for generating h^+, $^{\bullet}OH$ and $O^{2-\bullet}$ during the photocatalytic process. The higher removal percentage reduction in the caffeine degradation in the presence of N_2 indicates that $O^{2-\bullet}$ plays a more prominent role in photodegradation.

The adsorption kinetics and isotherm analysis were performed to evaluate the adsorption behavior of the material. The plots in Fig. S4(a) and (c)† show pseudo-first-order kinetic modeling at different pH and adsorbent dosages, respectively, with high correlation coefficients ($R^2 > 0.97$), confirming that the adsorption process follows pseudo-first-order kinetics, indicating chemisorption as the rate-limiting step. The Langmuir isotherm fitting shown in Fig. S4(b) and (d)† exhibits excellent linearity ($R^2 = 1$), suggesting monolayer adsorption on a homogeneous surface. The calculated Langmuir constants (K_L) further support the strong affinity of the adsorbate towards the adsorbent surface under varying experimental conditions.

Fig. S5a and b† display the alteration in zeta potential upon incorporating Mg into NiO, indicating enhanced surface basicity. This modification affects the photocatalyst's interaction with polar pollutants and facilitates reactive oxygen species (ROS) generation, ultimately improving its photocatalytic degradation performance. The point of zero charge (PZC) is the pH at which the zeta potential (surface potential) of a material is zero, *i.e.*, the surface carries no net electrical charge, and electrostatic interactions with charged species in solution are minimized. Fig. S5b and c† display the PZC for $MgNiO_2$ and NiO, respectively.

The PZC for a material is defined as the pH at which the net charge of the total particle surface is equal to zero (*i.e.*, concentration of H^+ is equal to OH^-).[41,42] From the obtained results, PZC for $MgNiO_2$ was around 7.9–8.0, and it was 7.4 for NiO. This means that for $MgNiO_2$, its surface shows a net positive charge at pH values less than 7.8 and a negative charge at pH values greater than 7.8. In the case of pure nickel oxide (PZC-7.4), its surface carries a net positive charge at pH values below 7.4 and a net negative charge at pH values above 7.4.

The incorporation of Mg into the NiO lattice increases the PZC from approximately 7.4 to around 7.9–8.0. This shift in the PZC indicates an increase in surface basicity due to the presence of Mg^{2+} ions (because of the more electropositive nature of Mg^{2+}), which enhance the surface's affinity for hydroxyl (–OH) group adsorption.

At pH < PZC (7.9–8.0), $MgNiO_2$ exhibits a positive net surface charge as the surrounding solution has an excess of H^+ ions undergoing surface protonation. OH_2^+ groups give the surface a positive charge, which is detected in zeta potential measurements, increasing electrostatic attraction for negatively charged or polar contaminants such as caffeine at low pH.[43,44]

As a result, the modified surface (now functionalized with –OH groups) exhibits enhanced electrostatic interactions with the pollutant, which is a polar molecule, directly influencing adsorption-driven photocatalytic performance under varying pH conditions. Caffeine, a polar molecule with functional groups such as carbonyl C=O and amide-like N–H groups, forms hydrogen bond interactions with surface hydroxyl (–OH) groups on $MgNiO_2$. Surface hydroxylation plays a critical role in photocatalytic pollutant degradation by enhancing the adsorption of polar contaminants containing N, O, and F elements through hydrogen bonding.[45]

At pH > PZC, $MgNiO_2$ shows a negative net surface charge because of an excess of OH^- ions in solution. These OH^- ions promote the deprotonation of surface –OH groups to give $–O^-$. Therefore, caffeine adsorption reduces due to repulsion, but ROS generation from –OH groups still continues upon light irradiation. The incorporation of Mg^{2+} creates oxygen vacancies or defect sites due to the size mismatch between Ni and Mg. Mg has a lower electronegativity (1.31) than Ni (1.88). Therefore, MgO bonds are more ionic and weaker than NiO bonds, which triggers the lattice to release oxygen and form vacancies, enhancing surface reactivity and photocatalytic performance.[46] These vacancies, along with surface hydroxylation, enhance the

$MgNiO_2$ ability in comparison with NiO for ROS generation, like $HO_2^{\bullet}$ and $^1O_2$, by providing more reactive hydroxyl groups for photocatalytic reactions.[47] These defects act as trap sites for photogenerated electrons or holes, reducing their chances of recombination. Mg introduces defects that promote charge separation by trapping photogenerated carriers, extending their lifetime for catalytic reactions.[48]

The presence of these hydroxyl radicals was further confirmed by the ESR studies presented in Fig. S5c.† The multiple well-resolved peaks observed in the spectrum are due to the interaction of the unpaired electron with nearby nuclei, confirming the presence of hydroxyl radicals in the system.

Next, the main $MgNiO_2$ surface parameters intervening in the caffeine photodegradation under visible light have been summarized. The interaction of caffeine with $MgNiO_2$ occurs through the OH-surface attached groups on $MgNiO_2$. The hydrophilic surface of $MgNiO_2$ is covered by $^-$OH groups present in diverse configurations on Mg and Ni. These $^-$OH groups assume different forms, most of them being covalent terminals, ionic terminals and ionic bridging and found on the $MgNiO_2$ bonding sites. A parameter controlling the density of –OH groups attached to $MgNiO_2$ is the surface potential of $MgNiO_2$. The two last points have not been investigated since they are beyond the scope of the present study. Full surface hydroxylation is noted as $MgNiO_2 + 2^{\bullet}OH_{ads} \rightarrow Mg(OH)_2 + Ni(OH)_2$. $MgNiO_2$ surface charges undergo surface migration leading to *redox* reactions under light irradiation. This reaction can be noted as $Mg^{+2}Ni^{+2}O_2{}^{-2} \rightarrow Mg^{+2}(O^{-2}H^{+1})_2 + Ni^{+2}(O^{-2}H^{+1})_2$.

The stability and reusability of the catalyst were examined by subjecting the used catalyst to multiple degradation cycles of caffeine under identical reaction parameters. The catalyst was initially collected, thoroughly washed with distilled water and then dried in an oven at 60 °C overnight. Subsequently, reusability studies were conducted. Remarkably, after repeated use of the catalyst for four cycles, the degradation decreased by only 4.4% (91.02%). This result highlights the stability of the catalyst and its ability to be reused multiple times without significant loss of efficacy. A comparative study of the catalyst used in this work with other catalysts reported in the literature is presented in Table 1.

3.7. Electrocatalytic OER studies, $MgNiO_2$ vacancies, and Tafel plots

Building on the excellent photocatalytic performance of $MgNiO_2$, the catalyst's potential was further explored for its performance in electrocatalytic applications. This dual approach enhances its potential for multifunctional applications, promoting sustainability in energy technologies, and broadening its industrial and technological relevance.[54] Subsequently, the OER was performed only for $MgNiO_2$ and not for NiO, considering the promising photocatalytic results exhibited by the catalyst ($MgNiO_2$) earlier. Linear sweep voltammetry (LSV) was employed to assess the electrocatalytic performance of $MgNiO_2$ in a 1.0 M KOH electrolyte. The results are presented in Fig. 6. A three-electrode system was used to conduct electrochemical studies, with LSV curves recorded for $MgNiO_2$ and the bare NF under similar experimental conditions. The OER activities of the catalyst are shown in Fig. 6a and b, clearly indicating that $MgNiO_2$ outperforms the bare NF. The overpotential for $MgNiO_2$ was 317 mV (1.54 V *vs.* RHE), whereas the bare NF registered an overpotential of 457 mV (1.68 V *vs.* RHE). This significant difference in overpotential at a current density of 10 mA cm^{-2} highlights the superior OER performance of $MgNiO_2$ compared to the bare NF. Table S1† compares the results obtained during this study with other previous studies reported in the literature. Furthermore, to fully understand the kinetic parameters, the Tafel plots were generated from the LSV curves using eqn (9), as illustrated in Fig. 6c:

$$\eta = b \log j + a \tag{9}$$

In the above equation, '*b*' and '*j*' represent the Tafel slope and current density, respectively. The calculated Tafel slopes for $MgNiO_2$ and bare Ni (NF) were determined to be 208 mV dec^{-1} and 324 mV dec^{-1}, respectively. In the reaction sequence below, the active site of the electrocatalyst is represented as "M". The theoretical Tafel slope values correspond to the potential OER mechanism in an alkaline medium and the associated reactions occurring are shown below (10)–(14):

$$M + OH^- \rightarrow MOH_{adsorption} + e^- \tag{10}$$

$$MOH + OH^- \rightarrow H_2O + MO + e^- \tag{11}$$

$$MO + OH^- \rightarrow MOOH + e^- \tag{12}$$

$$MOOH + OH^- \rightarrow H_2O + MOO + e^- \tag{13}$$

Table 1 Comparison of the synthesized $MgNiO_2$ catalyst with other reported materials

Process initial	Catalyst (g L^{-1})	Catalyst concentration	Pollutant concentration	Removal efficiency	Time (min)	Ref.
UV	Co-MCM41	200 mg L^{-1}	0.05 mM	98.00%	100	49
UV mercury lamp (400 W)	$ZnO–ZnAl_2O_4$	0.3 g L^{-1}	20 mg L^{-1}	97.32%	60	50
UV mercury lamp (400 W)	$Mg–ZnO–Al_2O_3$	0.6 g L^{-1}	20 mg L^{-1}	98.9%	70	51
Mercury vapor lamp (125 W)	Ag–ZnO	0.3 g	20 mg L^{-1}	70%	300	52
UV-C lamp	$BiVO_4$/rGO	Electrode (20.3 cm^2)	10 μmol L^{-1}	94.2%	480	53
Visible light	PVA–CuO	30 mg	20 mg L^{-1}	99.03%	80	6
White LED light (50 W)	**$MgNiO_2$**	**20 mg**	**20 mg L^{-1}**	**95.4%**	**180**	**This work**

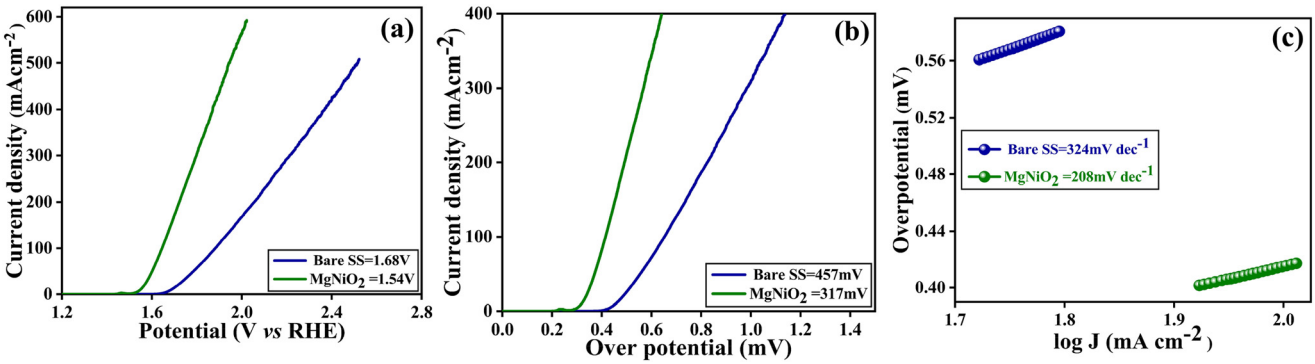

Fig. 6 Electrocatalytic OER studies of the as-synthesized $MgNiO_2$ catalyst and bare Ni foam (NF). (a and b) LSV overpotential data *vs.* RHE and (c) Tafel slopes.

$$MOO \rightarrow O_2 + M \quad (14)$$

The adsorption of OH^-, the cleavage of the O–H bond, and the subsequent desorption of O_2 seem to follow the theoretical Tafel slope values of 120 mV dec^{-1}, 30 mV dec^{-1}, and 20 mV dec^{-1}, respectively. These findings may provide the rationale for the synthesized catalyst presenting superior electrocatalytic OER activity. Oxygen vacancies play a crucial role in electrocatalytic OER studies, where a lower Tafel slope indicates a high density of oxygen vacancies for $MgNiO_2$. Table S1† indicates that the Tafel slope for $MgNiO_2$ is significantly higher than that of NiO_x-oxides. This provides further evidence for the effects of Mg when entering a Mg–Ni–O crystal structure. A schematic of the photocatalytic and electrocatalytic processes of the synthesized $MgNiO_2$ catalyst is shown in Fig. S4.†

The Nyquist plot shown in Fig. S6a† compares the charge transfer resistance of NiO and $MgNiO_2$ catalysts. The $MgNiO_2$ sample exhibits a smaller semicircle diameter than that of NiO, indicating a lower charge transfer resistance and improved electrical conductivity. This suggests that magnesium incorporation enhances the electron transport properties of NiO, facilitating faster charge transfer kinetics during the electrochemical reaction, which is beneficial for efficient electrocatalytic performance.

The cycling stability studies were conducted for a period of 22 h, and the same is presented in Fig. S6b.† This chronoamperometric curve demonstrates that the $MgNiO_2$ catalyst exhibits excellent long-term stability for the OER, with only a very slight increase in potential over 22 hours of continuous operation, confirming its durability and suitability for practical electrochemical applications. In addition, post-cycling characterization studies were also carried out to understand the stability or reusability of the material. HRTEM and XPS studies were used to analyse the material, and the same is provided in Fig. S7 and S8,† respectively.

The TEM analysis after electrolysis reveals that the $MgNiO_2$ nanoparticles retain their original granular morphology, indicating excellent structural stability during electrochemical operation. The bright-field TEM image in Fig. S7(a)† and the HAADF-STEM image in Fig. S7(b)† show uniformly dispersed nanoparticles without significant aggregation or structural collapse. The elemental mapping shown in Fig. S7(c–e)† confirms the homogeneous distribution of Mg, Ni and O throughout the sample, demonstrating that the compositional integrity of the material is well preserved even after electrolysis. The SAED pattern (f) displays distinct diffraction rings, suggesting that the crystalline nature of the $MgNiO_2$ nanoparticles remains intact after electrochemical cycling. Overall, these results confirm the robustness of $MgNiO_2$ nanoparticles under electrochemical conditions, maintaining both their granular structure and crystalline phase after electrolysis.

The XPS analysis after electrolysis confirms the chemical stability and retention of key surface states in the $MgNiO_2$ nanoparticles (Fig. S8†). In the Mg 1s spectrum (a), the presence of Mg–O (1301.2 eV), $Mg(OH)_2$ (1302.4 eV) and metallic Mg (1303.4 eV) indicates that magnesium remains largely in its original chemical environment with minor surface hydroxylation after electrolysis. The Ni 2p spectrum (b) shows characteristic peaks corresponding to $Ni(OH)_2$ (853.7 eV), NiO (855.4 eV) and NiOOH (861 eV), suggesting partial surface oxidation during electrolysis, probably due to electrochemical cycling, while the overall nickel oxidation states remain well-defined. The O 1s spectrum (c) shows dominant peaks assigned to lattice oxygen (O^{2-}) and surface hydroxyl species, further confirming the preservation of the oxide framework. These results demonstrate that the $MgNiO_2$ nanoparticles maintain their chemical integrity and surface composition after electrolysis, supporting their stability and suitability for repeated electrochemical operation.

4. Conclusions

This study demonstrated the effective visible-light-driven degradation of caffeine using granular $MgNiO_2$, emphasizing the critical role of the Mg–Ni–O lattice in promoting photocatalytic performance. Compared to pristine NiO, $MgNiO_2$ exhibited a narrowed band gap, enhanced light harvesting and improved charge carrier dynamics, as confirmed by PL and XPS analyses. The presence of Ni^{3+} and

highly oxidized Mg states contributed to increased surface reactivity and the generation of reactive oxygen species. Furthermore, $MgNiO_2$ displayed superior OER activity, attributed to its high density of oxygen vacancies and stable Mg–Ni–O crystalline framework. These findings underscore the dual applicability of $MgNiO_2$ in both environmental remediation and renewable energy technologies. However, its limited performance in the HER, probably due to surface passivation or poor proton adsorption, highlights a key limitation. Future work should focus on engineering surface defects, tuning the metal ratio or introducing co-catalysts to improve its bifunctional electrocatalytic behaviour. Additionally, scaling studies, stability under real-water matrices and pollutant mixtures should be explored to validate its practical deployment in water treatment and electrochemical devices.

Data availability

The data supporting the findings of this study are available from the corresponding author upon reasonable request.

Conflicts of interest

There are no conflicts of interest with the authors or any other person with regard to the reported work.

References

1 S. Ibrahim, A. Muhammad, A. S. Tanko, A. Abubakar, H. Ibrahim, M. Y. Shukor and S. A. Ahmad, *Bayero Journal of Pure and Applied Sciences*, 2015, **8**, 138–144.
2 R. Raj, A. Tripathi, S. Das and M. Ghangrekar, *Case Stud. Chem. Environ. Eng.*, 2021, **4**, 100129.
3 Y. M. Correa-Navarro, G.-D. López, C. Carazzone, L. Giraldo and J. C. Moreno-Piraján, *ACS Omega*, 2023, **8**, 38905–38915.
4 F. Escalona-Durán, D. R. da Silva, C. A. Martínez-Huitle and P. Villegas-Guzman, *Chemosphere*, 2020, **253**, 126599.
5 N. Gadi, N. C. Boelee and R. Dewil, *Sustainability*, 2022, **14**, 14313.
6 V. D. Kumar, S. Kumari, K. Balaji, A. A. Khan, C. Ravikumar, B. Basavaraja, M. Santosh and S. Rtimi, *Chem. Eng. J.*, 2023, **462**, 142187.
7 F. Hosseini, A. A. Assadi, P. Nguyen-Tri, I. Ali and S. Rtimi, *Surf. Interfaces*, 2022, **32**, 102078.
8 G. Mamba, P. Mafa, V. Muthuraj, A. Mashayekh-Salehi, S. Royer, T. Nkambule and S. Rtimi, *Mater. Today Nano*, 2022, **18**, 100184.
9 C. M. Reyes and M. C. Cornelis, *Nutrients*, 2018, **10**, 1772.
10 F.-Y. Liu, Y.-R. Jiang, C.-C. Chen and W. W. Lee, *Catal. Today*, 2018, **300**, 112–123.
11 C.-W. Siao, W.-L. W. Lee, Y.-M. Dai, W.-H. Chung, J.-T. Hung, P.-H. Huang, W.-Y. Lin and C.-C. Chen, *J. Colloid Interface Sci.*, 2019, **544**, 25–36.
12 V. Dileepkumar, K. Balaji, R. Vishwanatha, B. Basavaraja, S. Ashoka, I. M. Al-Akraa, M. Santosh and S. Rtimi, *Chem. Eng. J.*, 2022, **446**, 137023.
13 Y. Sneha, J. S. Prabagar, T. Tenzin, B. Shahmoradi, K. Wantala, S. Rtimi, A. Maleki, D. B. Das and H. P. Shivaraju, *J. Environ. Chem. Eng.*, 2023, **11**, 110950.
14 M. Imran, E.-B. Kim, D.-H. Kwak and S. Ameen, *Sensors*, 2023, **23**, 7910.
15 M. S. Santosh, P. Sherugar, K. R. Balaji, A. Ahmad Khan, M. Padaki, S. Klyamkin, E. Galim, P. Singh and S. Rtimi, *Chem. Eng. Sci.*, 2024, **293**, 120074.
16 W. Guo, S. Wang, Y. Liu, G. Gao, L. Lin, Y. Zhang, M. Fan, J. Ren, J. Lin and Q. Luo, *J. Power Sources*, 2023, **585**, 233658.
17 H. Gan, L. Li, P. Qiu, M. Cui, J. Sun, Y. Xia and W. Zhu, *Electrochim. Acta*, 2025, 145728.
18 N. A. Ali, N. H. Idris, M. F. M. Din, M. S. Yahya and M. Ismail, *J. Alloys Compd.*, 2019, **796**, 279–286.
19 G. Allaedini, P. Aminayi and S. M. Tasirin, *AIP Adv.*, 2015, **5**, 077161.
20 P. Ponnusamy, S. Agilan, N. Muthukumarasamy, T. Senthil, G. Rajesh, M. Venkatraman and D. Velauthapillai, *Mater. Charact.*, 2016, **114**, 166–171.
21 A. Patterson, *Phys. Rev.*, 1939, **56**, 978.
22 N. Setoudeh, C. Zamani and M. Sajjadnejad, *J. Ultrafine Grained Nanostruct. Mater.*, 2017, **50**, 51–59.
23 S. Brunauer, L. S. Deming, W. E. Deming and E. Teller, *J. Am. Chem. Soc.*, 1940, **62**, 1723–1732.
24 C. Chizallet, G. Costentin, M. Che, F. Delbecq and P. Sautet, *J. Am. Chem. Soc.*, 2007, **129**, 6442–6452.
25 J. M. Ramos, M. Cruz, A. C. Costa Jr, O. Versiane and C. A. T. Soto, *ScienceAsia*, 2011, **37**, 247–255.
26 Y. Idemoto, T. Takahashi, N. Ishida, M. Nakayama and N. Kitamura, *Inorg. Chem.*, 2019, **58**, 5664–5670.
27 N. Ali, N. Idris, M. M. Din, M. Yahya and M. Ismail, *J. Alloys Compd.*, 2019, **796**, 279–286.
28 M. Dekermenjian, A. P. Ruediger and A. Merlen, *RSC Adv.*, 2023, **13**, 26683–26689.
29 A. Khalaf, R. Saghir, A. Abdallah, M. Noun and R. Awad, *Appl. Phys. A: Mater. Sci. Process.*, 2024, **130**, 691.
30 H. Liu, P. Da Costa, H. B. H. Taief, M. Benzina and M. Gálvez, *RSC Adv.*, 2018, **8**, 19627–19634.
31 A. Posada-Borbon, N. Bosio and H. Grönbeck, *Surf. Sci.*, 2021, **705**, 121761.
32 K. V. Chandekar, B. Palanivel, F. H. Alkallas, A. B. G. Trabelsi, A. Khan, I. M. Ashraf, S. AlFaify and M. Shkir, *J. Phys. Chem. Solids*, 2023, **178**, 111345.
33 A. Fujishima, X. Zhang and D. A. Tryk, *Surf. Sci. Rep.*, 2008, **63**, 515–582.
34 A. Mills and J. Wang, *J. Photochem. Photobiol., A*, 1999, **127**, 123–134.
35 J. Tong, D. Wang, D. Wang, F. Xu, R. Duan, D. Zhang, J. Fan and B. Dong, *Langmuir*, 2019, **36**, 6930–6937.
36 H. Zhang, C. Xie, L. Chen, J. Duan, F. Li and W. Liu, *Water Res.*, 2023, **229**, 119392.
37 P. Attri, Y. H. Kim, D. H. Park, J. H. Park, Y. J. Hong, H. S. Uhm, K.-N. Kim, A. Fridman and E. H. Choi, *Sci. Rep.*, 2015, **5**, 1–8.
38 F. J. Sevilla and M. Sandoval, *Phys. Rev. E: Stat., Nonlinear, Soft Matter Phys.*, 2015, **91**, 052150.

39 A. Farah and C. M. Donangelo, *Braz. J. Plant Physiol.*, 2006, **18**, 23–36.
40 X. Zhao, Y. Su, X. Qi and X. Han, *ACS Sustainable Chem. Eng.*, 2017, **5**, 6148–6158.
41 E. N. Bakatula, D. Richard, C. M. Neculita and G. J. Zagury, *Environ. Sci. Pollut. Res.*, 2018, **25**, 7823–7833.
42 E. McCafferty, *Electrochim. Acta*, 2010, **55**, 1630–1637.
43 Z. H. Athab, A. F. Halbus, S. B. Mohammed, A. J. Atiyah, H. I. Ismael, N. S. Saddam, S. J. Baqir, H. F. Alesary, S. Algburi and N. Al-Ansari, *Sci. Rep.*, 2024, **14**, 4032.
44 N. Wang, C. Hsu, L. Zhu, S. Tseng and J.-P. Hsu, *J. Colloid Interface Sci.*, 2013, **407**, 22–28.
45 T. Cui, Y. Su, X. Fu, Y. Zhu and Y. Zhang, *J. Alloys Compd.*, 2022, **921**, 165931.
46 S. Zhao, L. Gao, C. Lan, S. S. Pandey, S. Hayase and T. Ma, *RSC Adv.*, 2016, **6**, 31968–31975.
47 S. Zhao, L. Gao, C. Lan, S. S. Pandey, S. Hayase and T. Ma, *RSC Adv.*, 2016, **6**, 43034–43040.
48 F. Bi, Q. Meng, Y. Zhang, H. Chen, B. Jiang, H. Lu, Q. Liu, H. Zhang, Z. Wu and X. Weng, *Nat. Commun.*, 2025, **16**, 851.
49 F. Qi, W. Chu and B. Xu, *Appl. Catal., B*, 2013, **134**, 324–332.
50 A. Elhalil, R. Elmoubarki, A. Machrouhi, M. Sadiq, M. Abdennouri, S. Qourzal and N. Barka, *J. Environ. Chem. Eng.*, 2017, **5**, 3719–3726.
51 A. Elhalil, R. Elmoubarki, M. Farnane, A. Machrouhi, M. Sadiq, F. Mahjoubi, S. Qourzal and N. Barka, *Environ. Nanotechnol., Monit. Manage.*, 2018, **10**, 63–72.
52 L. N. B. Almeida, J. M. T. A. Pietrobelli, G. G. Lenzi and O. A. A. Santos, *Braz. Arch. Biol. Technol.*, 2020, **63**, e20180614.
53 T. M. Prado, F. L. Silva, A. Carrico, M. R. de Vasconcelos Lanza, O. Fatibello-Filho and F. C. Moraes, *Mater. Res. Bull.*, 2022, **145**, 111539.
54 J. Huang, Y. Su, Z. Qian, M. Wu, Y. Xie and C. Zeng, *Dalton Trans.*, 2025, **54**(9), 2495–2502.